nature nanotechnology

LETTERS

https://doi.org/10.1038/s41565-021-01014-y

Check for updates

Coexisting ferromagnetic–antiferromagnetic state in twisted bilayer CrI_3

Yang Xu[1,2], Ariana Ray[3], Yu-Tsun Shao[1], Shengwei Jiang[3], Kihong Lee[3], Daniel Weber[4], Joshua E. Goldberger[4], Kenji Watanabe[5], Takashi Taniguchi[6], David A. Muller[1,7], Kin Fai Mak[1,3,7] ✉ and Jie Shan[1,3,7] ✉

Moiré engineering[1–3] of van der Waals magnetic materials[4–9] can yield new magnetic ground states via competing interactions in moiré superlattices[10–13]. Theory predicts a suite of interesting phenomena, including multiflavour magnetic states[10], non-collinear magnetic states[10–13], moiré magnon bands and magnon networks[14] in twisted bilayer magnetic crystals, but so far such non-trivial magnetic ground states have not emerged experimentally. Here, by utilizing the stacking-dependent interlayer exchange interactions in two-dimensional magnetic materials[15–18], we demonstrate a coexisting ferromagnetic (FM) and antiferromagnetic (AF) ground state in small-twist-angle CrI_3 bilayers. The FM–AF state transitions to a collinear FM ground state above a critical twist angle of about 3°. The coexisting FM and AF domains result from a competition between the interlayer AF coupling, which emerges in the monoclinic stacking regions of the moiré superlattice, and the energy cost for forming FM–AF domain walls. Our observations are consistent with the emergence of a non-collinear magnetic ground state with FM and AF domains on the moiré length scale[10–13]. We further employ the doping dependence of the interlayer AF interaction to control the FM–AF state by electrically gating a bilayer sample. These experiments highlight the potential to create complex magnetic ground states in twisted bilayer magnetic crystals, and may find application in future gate-voltage-controllable high-density magnetic memory storage.

There is a one-to-one correspondence between the stacking structure and the magnetic ground state in CrI_3 bilayers (Fig. 1b): the monoclinic (M) phase supports an A-type antiferromagnetic (AF) ground state with two AF-coupled ferromagnetic (FM) monolayers; and the rhombohedral (R) phase supports an FM ground state[15,16,19,20]. The magnetic easy axis is out-of-plane. There are both M and R regions in the triangular moiré superlattice of a twisted bilayer (Fig. 1a). The competing interlayer AF and FM interactions on the moiré length scale can induce non-trivial magnetic ground states with coexisting AF and FM domains (Fig. 1b)[10–14]. These states are expected to emerge when the energy gain from forming AF domains in the M regions exceeds the energy cost from forming domain walls. Since the energy gain scales with the area of the moiré unit cell, whereas the energy cost scales with the moiré period, such a coexisting FM–AF state is favoured below a critical twist angle[10]. This ideal picture could be modified in samples with very small twist angles, for instance, by lattice reconstruction[21] that favours the most stable structure, the (FM) R phase[15,16,19].

We fabricate twisted CrI_3 bilayers by the tear-and-stack method (Methods and Extended Data Fig. 1), which has been widely used to make twisted bilayer graphene samples[22–24]. A series of samples with varying target twist angle θ has been studied. The twist-angle accuracy is ±0.5° on average. All samples are encapsulated between hexagonal boron nitride (hBN) substrates to prevent environmental degradation. The moiré structure of a small number of samples was verified by standard four-dimensional (4D) scanning transmission electron microscopy (STEM). Very thin hBN encapsulation layers (<5 nm) and substrates (8-nm-thick amorphous SiO_2) were required to obtain TEM images (Extended Data Fig. 3). We have also fabricated a number of dual-gated field-effect devices to continuously tune the interlayer AF interaction by varying the doping level in CrI_3 (refs. [25,26]).

Figure 1c shows the electron diffraction pattern of sample 1 with $\theta = 1.5°$. Diffraction peaks from both hBN and CrI_3 are observed. Figure 1d–f shows dark-field images obtained by selecting one of the third-order diffraction peaks of the CrI_3 bilayer (circled in Fig. 1c). A clear moiré stripe pattern with a periodicity of one-third of the moiré period $a_M/3 = 6.1 \pm 0.9$ nm is seen. Each image is related to the other by a 60° rotation. The real-space moiré pattern can be constructed by superimposing the three images (Extended Data Figure 3). Using the measured a_M, we determine $\theta = 2\sin^{-1}\left(\frac{a}{2a_M}\right) \approx 2.2° \pm 0.3°$ ($a = 0.687$ nm is the in-plane lattice constant of CrI_3). (Here the error for θ of sample 1 is propagated from that for a_M.) The dark-field images in a larger field-of-view and for another sample are shown in Extended Data Figs. 4 and 5. These results verify the formation of moiré structures in twisted bilayer CrI_3 and the expected twist-angle accuracy.

We probe the magnetic ground state by magnetic circular dichroism (MCD) measurements. The MCD is linearly proportional to the out-of-plane magnetization. However, a direct comparison of the absolute MCD for different samples is not appropriate because of the different local field factors from different substrate thicknesses. Unless otherwise specified, all measurements were performed at 4 K.

Figure 2a–d shows the MCD as a function of out-of-plane magnetic field B for four bilayer samples. (Extended Data Figs. 3, 4, 7 and 8 show results from additional samples and correlated STEM

[1]School of Applied and Engineering Physics, Cornell University, Ithaca, NY, USA. [2]Beijing National Laboratory for Condensed Matter Physics, Institute of Physics, Chinese Academy of Sciences, Beijing, China. [3]Department of Physics, Cornell University, Ithaca, NY, USA. [4]Department of Chemistry and Biochemistry, The Ohio State University, Columbus, OH, USA. [5]Research Center for Functional Materials, National Institute for Materials Science, Tsukuba, Japan. [6]International Center for Materials Nanoarchitectonics, National Institute for Materials Science, Tsukuba, Japan. [7]Kavli Institute at Cornell for Nanoscale Science, Ithaca, NY, USA. ✉e-mail: kinfai.mak@cornell.edu; jie.shan@cornell.edu

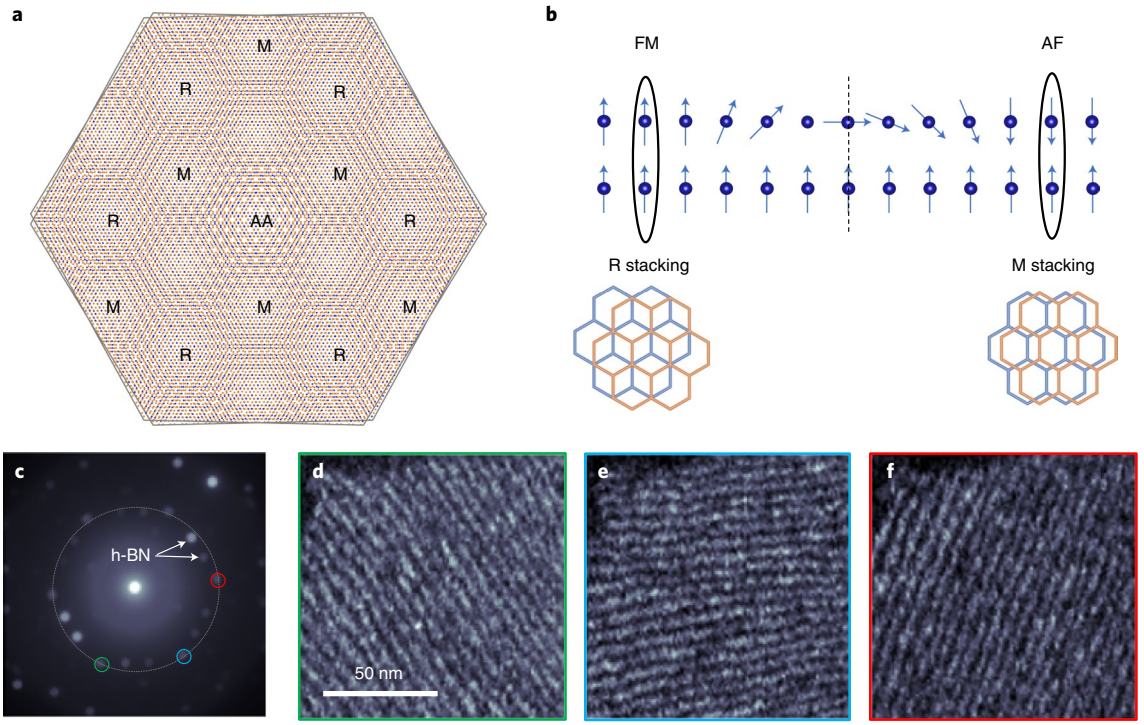

Fig. 1 | Moiré superlattice structure of twisted bilayer CrI_3. **a**, Moiré superlattice structure of a small-twist-angle CrI_3 bilayer. R, M and AA denote rhombohedral, monoclinic and AA stacking, respectively. **b**, Schematic illustration of a magnetic domain wall formed between the R- and M-stacking regions. Balls and arrows denote the spins of magnetic ions. Blue and orange denote two adjacent CrI_3 monolayers. **c**, Electron-beam diffraction pattern from a small-twist-angle CrI_3 bilayer, down the <001> zone axis (perpendicular to the sample surface). The two arrows indicate the diffraction spots (six pairs in total) from the top and bottom hBN capping layers. The large dashed circle tracks the <300> diffraction peaks for CrI_3. **d**–**f**, Real-space dark-field moiré fringe patterns: the peaks in **c** circled in green, blue and red are the dark-field masks for the patterns in **d**–**f**, respectively.

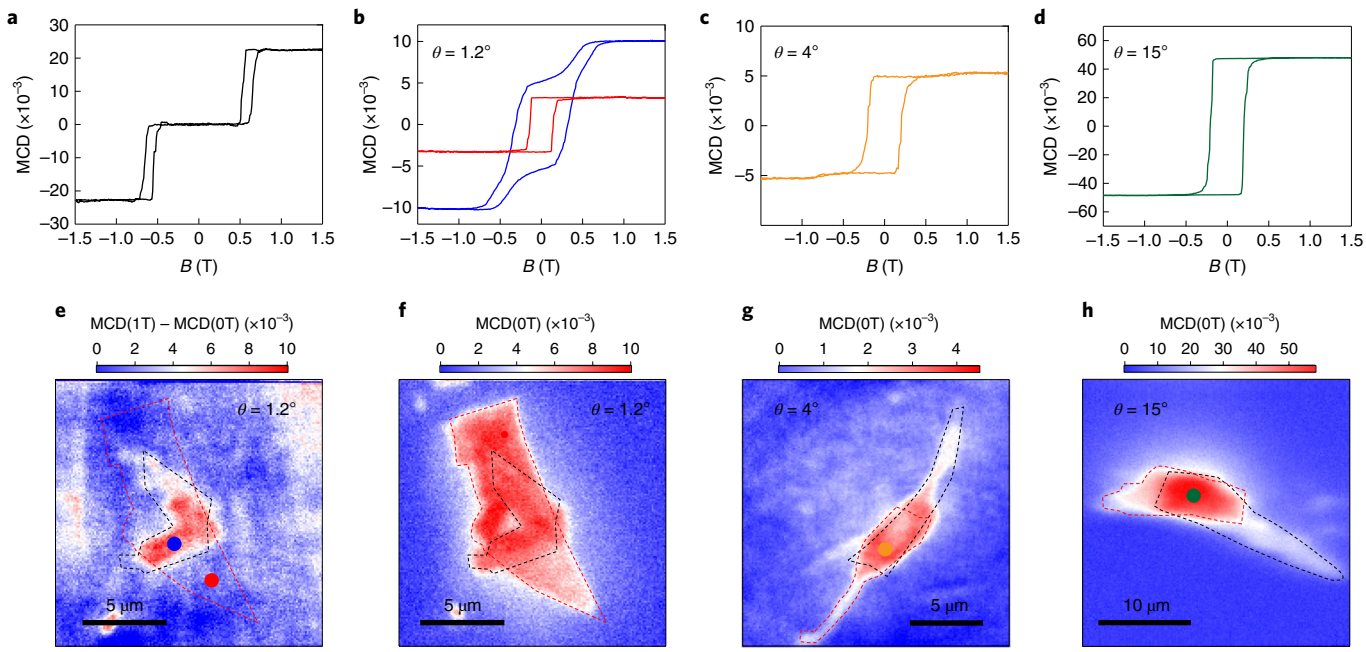

Fig. 2 | MCD microscopy of twisted bilayer CrI_3. **a**–**d**, Magnetic-field dependence of MCD of a natural bilayer CrI_3 (**a**) and twisted bilayer CrI_3 with twist angle 1.2° (**b**), 4° (**c**) and 15° (**d**). The MCD of an isolated monolayer CrI_3 is shown in **b** for comparison (red). Coexistence of AF and FM contributions is evident at small twist angles. **e**, Image of MCD(1T) – MCD(0T) for the 1.2° sample, illustrating the AF fraction of the sample. Non-zero contrast is observed only in the twisted bilayer region. **f**–**h**, MCD images at $B = 0$ T for the 1.2° (**f**), 4° (**g**) and 15° (**h**) samples (samples are polarized at 1 T prior to the MCD measurement), showing the FM fraction of the samples. In all images the dashed black and red lines outline the constituent monolayer regions. The coloured dots denote the locations of the MCD measurements of the same colour in **b**–**d**. The upper part of the designed twisted bilayer in **e** and **f** contains patches of only one monolayer (red dashed line) because parts of the second monolayer (black dashed line) broke off in the fabrication process, giving rise to a reduced MCD contrast in **e**.

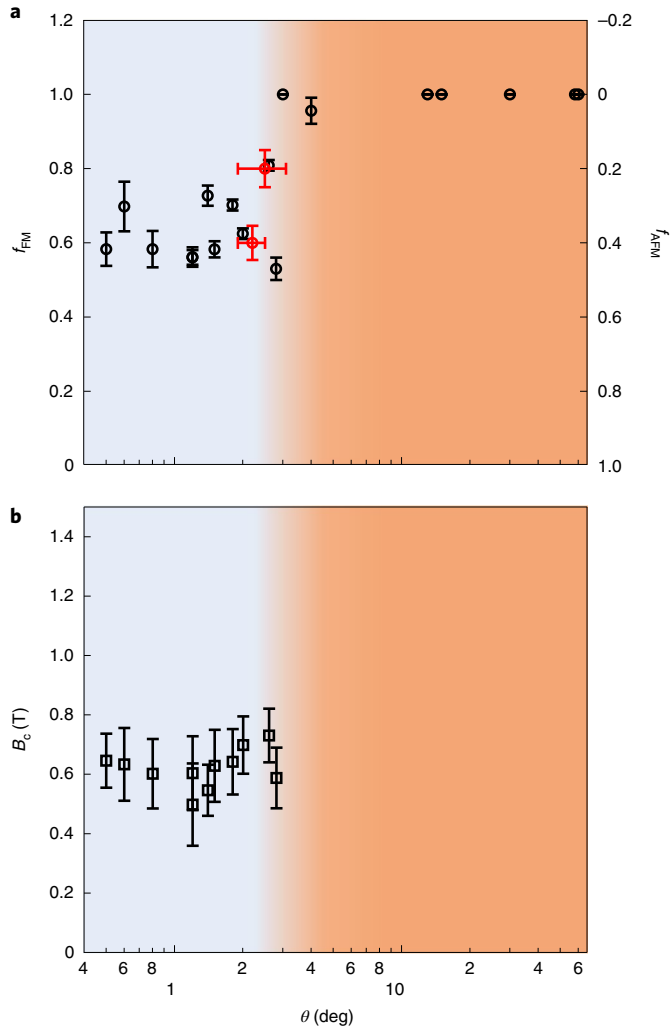

Fig. 3 | Twist-angle dependence. a, The FM and AF fractions, f_{FM} (left axis) and f_{AF} (right axis), as a function of target twist angle θ for all measured samples. The vertical error bars are estimated from measurements at different sample locations and indicate the spatial inhomogeneity. The twist-angle uncertainty is estimated to be about 0.5° (not shown); it is characterized for two samples (red circle) by STEM. At small twist angles ($\theta \lesssim 3°$), $f_{FM} < 1$ indicates a mixed AF–FM ground state; a pure FM ground state is observed at $\theta \gtrsim 4°$. **b**, Twist-angle dependence of the spin-flip transition field B_c. The vertical error bars are estimated from the field span of the spin-flip transition.

and MCD studies.) A natural bilayer with M stacking (Fig. 2a) is included as a reference. Its MCD is negligible until the field reaches the critical value $B_c \approx 0.6$ T for the spin-flip transition; the behaviour is fully consistent with the reported A-type AF state[5,27]. Also included is the MCD from an isolated monolayer (Fig. 2b, red line); it shows the expected FM loop. The magnetic response is different in the 1.2° twist sample (Fig. 2b). Both AF and FM behaviours are present. In addition to the spin-flip transition near $B_c \approx 0.5$–0.6 T, a FM loop centred at zero field emerges and is continuously connected to the spin-flip transition. The behaviour is distinct from a simple superposition of an independent FM and AF response; it is in good agreement with the theoretical magnetic response of twisted bilayer CrI_3 with moiré magnetic textures[13]. Our result is therefore inconsistent with large-scale uncorrelated AF and FM domains (Methods).

As θ increases, the AF contribution quickly diminishes: a very small AF contribution remains in the 4° twist sample; the response is purely FM in the 15° twist sample. We denote the fraction of the FM and AF domains in the sample by $f_{FM} \approx \frac{MCD(0T)}{MCD(1T)}$ and $f_{AF} \approx 1 - f_{FM}$, respectively. (We have ignored the domain walls; they are estimated in Methods to be narrow compared to the moiré period at low temperatures.) The θ dependence of f_{FM} is summarized in Fig. 3. The AF–FM coexistence disappears at a critical angle $\theta_c \approx 3°$, above which only FM response is observed. Below θ_c, it is found that f_{FM}, B_c and the FM coercive field are all weakly angle dependent.

We characterize the magnetic spatial homogeneity by MCD imaging. Figure 2e,f shows MCD(1T) − MCD(0T) and MCD(0T), respectively, which represent the AF and FM contributions in the 1.2° twist sample (the boundary of each CrI_3 monolayer is roughly marked by dashed curves). We observe $f_{AF} \approx 0$ in the isolated monolayer regions as expected, and a finite f_{AF} in most twisted bilayer regions. The FM contribution in the bilayer regions is comparable to that of the isolated monolayers. The result shows homogeneous AF–FM coexistence. On the other hand, the AF contribution is absent over the entire sample for $\theta > \theta_c$ (Extended Data Fig. 8), and the FM signal is nearly double that of the isolated monolayer regions (Fig. 2g for $\theta = 4°$; Fig. 2h for $\theta = 15°$).

We further examine the temperature dependence of the magnetic response of the 1.2° twist sample. Figure 4a is a contour of the MCD versus temperature and field scanned from −1.5 T to 1.5 T. Figure 4b shows the field dependence of the MCD at varying temperatures. The fractions f_{FM} and f_{AF} are nearly temperature independent for the entire temperature range. Upon cooling, the coercive field of the FM contribution increases monotonically (Fig. 4c). This is consistent with the behaviour of monolayer CrI_3. The spin-flip transition field B_c first increases and then decreases slightly as temperature decreases (Fig. 4c). This deviates from the monotonic increase of B_c upon cooling in natural bilayer CrI_3 (Extended Data Fig. 9). For samples with $\theta > \theta_c$ we measure the temperature-dependent magnetic a.c. susceptibility, which shows a single diverging peak, indicating a fully coupled bilayer and a Curie temperature substantially higher than the monolayers (Extended Data Fig. 6).

The distinct behaviour of twisted bilayers and FM monolayers, including the presence of AF contributions for $\theta < \theta_c$ and higher Curie temperatures for $\theta > \theta_c$, is a manifestation of the interlayer magnetic interactions in twisted bilayers. The observed nearly constant coercive field does not contradict this conclusion because the coercive field is mainly determined by the magnetic anisotropy and sample temperature. The observed AF–FM coexistence and the distinct magnetic response in small-twist-angle CrI_3 bilayers indicate the formation of small-scale, interacting AF and FM domains. Furthermore, the systematic twist-angle dependence in Fig. 3 and the consistent behaviour observed in multiple samples suggest that external origins such as strain and other disorders are unlikely.

Our results are consistent with the proposed non-collinear magnetic ground state driven by competing magnetic interactions in a moiré superlattice[10]. The moiré superlattice of twisted CrI_3 bilayers contains spatially modulated M and R stacking structures (Fig. 1a), which support AF and FM interlayer exchange, respectively. Because the interlayer FM exchange in the R phase is substantially stronger than the interlayer AF exchange in the M phase[19], we only need to consider the competition between the formation of AF domains and AF–FM domain walls. The energy gain per moiré unit cell from forming AF domains in the M regions, $\sim 2 f_{AF} \left(\frac{a_M}{a}\right)^2 J_\perp$, scales with a_M^2. The energy cost per moiré unit cell from forming AF–FM domain walls near the M–R stacking boundaries, $\sim \pi \left(\frac{a_M}{a}\right) \sqrt{J_\parallel (K + 2J_\perp)}$, scales with a_M (Methods). Here $J_\perp \approx 0.1$ meV and $J_\parallel \approx 2$ meV are the interlayer AF[5,27] and the intralayer FM[28] exchange constants, respectively, and $K \approx 0.3$ meV is the single-ion magnetic anisotropy energy[29]. The different scaling of the two energy terms with a_M guarantees that at small twist angles the

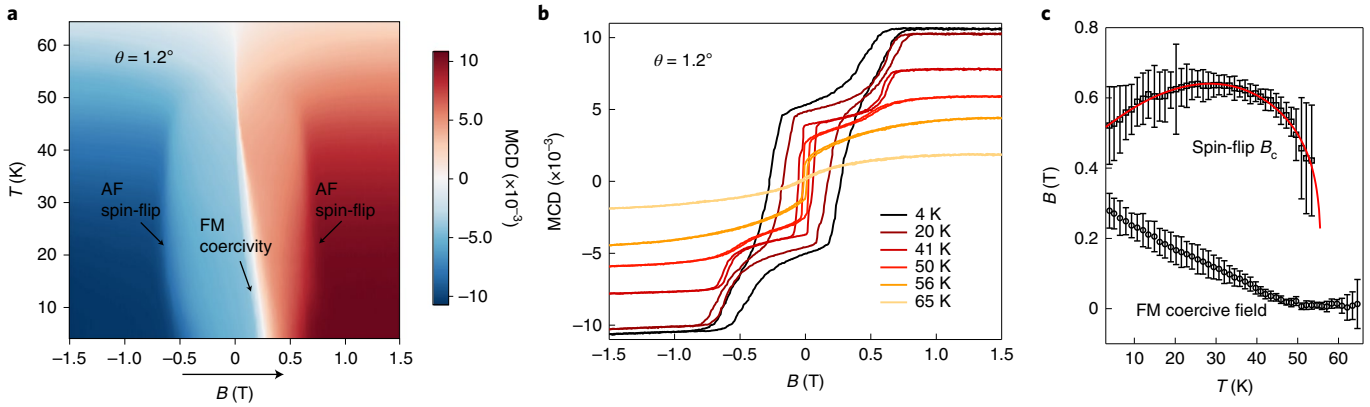

Fig. 4 | Temperature dependence. a, MCD as a function of temperature (at 1.2 K intervals) and magnetic field (sweeping from negative to positive) for a 1.2° twist bilayer CrI_3. **b**, Magnetic-field dependence of the MCD (for both forward and backward sweeps) at representative temperatures for the same sample. **c**, The extracted spin-flip transition field B_c (top) and the FM coercive field (bottom) as function of temperature. B_c is the average spin-flip transition field between forward and backward sweeps. The red curve is a fit to B_c using the model described in the main text. The vertical error bars are estimated from the field span of the magnetic transitions.

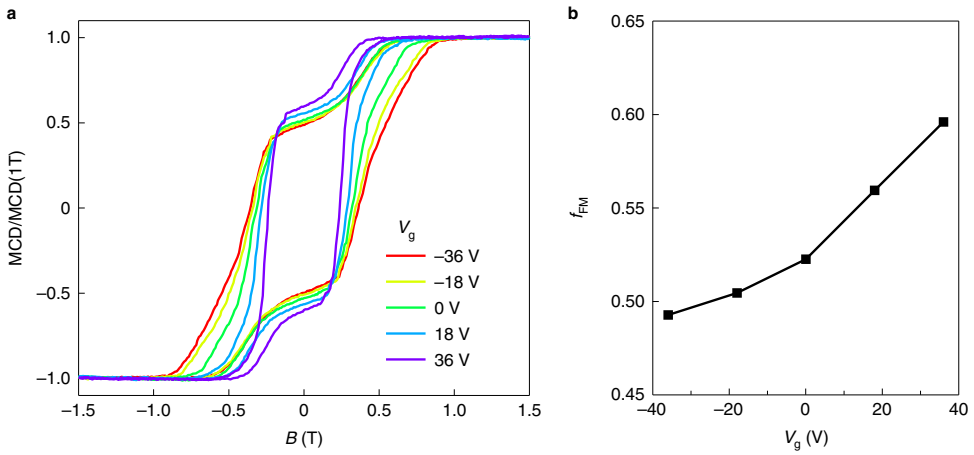

Fig. 5 | Gate control of the non-collinear magnetic state. a, MCD (normalized to 1 at large fields) as a function of magnetic field at selected gate voltages (V_g). V_g is the total gate voltage applied symmetrically to the top and bottom gates. **b**, FM fraction f_{FM} as a function of V_g. The error bar is smaller than the size of the data points.

energy gain from forming AF domains wins and a magnetic ground state with spatially modulated AF and FM regions emerges (Fig. 1b). The critical twist angle $\theta_c \sim \frac{f_{AF}J_\perp}{\sqrt{J_\parallel(K+2J_\perp)}} \approx 3°$ can be estimated by equating the two energy terms. The value is consistent with a recent numerical study[30].

Above θ_c, a collinear FM ground state is preferred. The transition from a coexisting FM–AF state to a collinear FM state can be continuous (for small $K/J_\perp$) or abrupt (for large $K/J_\perp$)[10]. In the continuous-phase-transition scenario, an intermediate non-collinear state with spins flop from the out-of-plane to the in-plane direction is also expected. In CrI_3 with large magnetic anisotropy ($K/J_\perp \approx 3$), the intermediate state has a high energy cost and an abrupt transition is favoured. This is consistent with experiment, in which spin-flip transitions are observed in all small-twist-angle bilayers. Because of the large magnetic anisotropy, the domain wall width is small compared to a_M (Methods) so that B_c is weakly angle dependent for $\theta < \theta_c$ (Fig. 3).

The non-monotonic temperature dependence of B_c is also a manifestation of the competing magnetic interactions. In natural bilayer CrI_3 with M stacking, the spin-flip transition occurs at $B_c \approx \frac{2J_\perp}{3\mu_B}$ (ref. [27]), at which the Zeeman energy gain of the FM state ($3\mu_B B$) overcomes the interlayer AF exchange energy cost ($2J_\perp$). Here μ_B is the Bohr magneton and each Cr ion carries $3\mu_B$. In twisted bilayer CrI_3, the presence of AF and FM domains lowers the energy cost for the spin-flip transition by the domain wall energy and gives $B_c \approx \frac{2f_{AF}J_\perp - \pi\left(\frac{a}{a_M}\right)\sqrt{J_\parallel(K+2J_\perp)}}{f_{AF}(3\mu_B)}$ (Methods). The exchange constants $J_\parallel$, $J_\perp \propto t^\alpha$ (with $\alpha < 1$) and the anisotropy energy $K \propto t^\beta$ (with $\beta > 1$) show distinct scaling with the reduced temperature $t = \frac{T_c - T}{T_c}$ (T_c is the critical temperature)[30–32]. Using $\alpha = 0.22$ (ref. [28]) for both $J_\parallel$ and $J_\perp$ and $\beta = 2.3$, we can reproduce the observed non-monotonic temperature dependence of B_c in Fig. 4c (red line).

Finally, we demonstrate gate control of the FM–AF state. Figure 5a shows the magnetic-field dependence of MCD (normalized by the saturated value at 1 T) at varying gate voltages for the 1.2° twist sample. With increasing gate voltage (corresponding to electron doping), B_c decreases by as much as ~50% while the FM loop is little affected. The result shows that the primary effect of

electron doping is to weaken the interlayer AF exchange $J_\perp$ in the M regions, consistent with earlier reports on natural bilayer CrI_3 (refs. [25,26]). Meanwhile, the remnant magnetization as manifested by $MCD(0T) \propto f_{FM}$ increases by ~10% with gating (Fig. 5b). (Extended Data Fig. 10 shows a similar result from another device.) Such an increase reflects shrinkage of the AF domains (or equivalently, expansion of the FM domains) as $J_\perp$ is weakened. At sufficiently high electron doping densities, where $J_\perp$ becomes smaller than the critical value $J_{\perp c} \approx \theta\sqrt{J_\parallel K}/f_{AF}$ (Methods), the energy gain from forming AF domains would be overcome by the energy cost of forming AF–FM domain walls, and an abrupt quantum phase transition from an FM–AF state to a collinear FM state is expected[10]. Tuning $J_\perp$ by electron doping in a sample with fixed θ is therefore similar to varying θ while keeping $J_\perp$ constant (Fig. 3). Future studies with higher electron doping densities or samples very close to θ_c will provide a promising route to achieve a voltage-induced transition.

In conclusion, we have realized moiré superlattices in twisted CrI_3 bilayers and demonstrated a new magnetic ground state with coexisting FM and AF orders, which can be further tuned by either twist-angle or electrical gating. Our results support the formation of AF and FM domains on the moiré length scale from competing interlayer exchange interactions and are consistent with the predictions of a spin model for twisted bilayer magnetic materials[10–14]. High-resolution and high-sensitivity magnetic imaging is warranted to directly demonstrate the moiré magnetic textures in future studies.

Online content

Any methods, additional references, Nature Research reporting summaries, source data, extended data, supplementary information, acknowledgements, peer review information; details of author contributions and competing interests; and statements of data and code availability are available at https://doi.org/10.1038/s41565-021-01014-y.

Received: 16 May 2021; Accepted: 20 September 2021;
Published online: 29 November 2021

References

1. Andrei, E. Y. & MacDonald, A. H. Graphene bilayers with a twist. *Nat. Mater.* **19**, 1265–1275 (2020).
2. Balents, L., Dean, C. R., Efetov, D. K. & Young, A. F. Superconductivity and strong correlations in moiré flat bands. *Nat. Phys.* **16**, 725–733 (2020).
3. Kennes, D. M. et al. Moiré heterostructures as a condensed-matter quantum simulator. *Nat. Phys.* **17**, 155–163 (2021).
4. Gong, C. et al. Discovery of intrinsic ferromagnetism in two-dimensional van der Waals crystals. *Nature* **546**, 265–269 (2017).
5. Huang, B. et al. Layer-dependent ferromagnetism in a van der Waals crystal down to the monolayer limit. *Nature* **546**, 270–273 (2017).
6. Burch, K. S., Mandrus, D. & Park, J.-G. Magnetism in two-dimensional van der Waals materials. *Nature* **563**, 47–52 (2018).
7. Gong, C. & Zhang, X. Two-dimensional magnetic crystals and emergent heterostructure devices. *Science* **363**, eaav4450 (2019).
8. Mak, K. F., Shan, J. & Ralph, D. C. Probing and controlling magnetic states in 2D layered magnetic materials. *Nat. Rev. Phys.* **1**, 646–661 (2019).
9. Gibertini, M., Koperski, M., Morpurgo, A. F. & Novoselov, K. S. Magnetic 2D materials and heterostructures. *Nat. Nanotechnol.* **14**, 408–419 (2019).
10. Hejazi, K., Luo, Z.-X. & Balents, L. Noncollinear phases in moiré magnets. *Proc. Natl Acad. Sci. USA* **117**, 10721 (2020).
11. Tong, Q., Liu, F., Xiao, J. & Yao, W. Skyrmions in the Moiré of van der Waals 2D magnets. *Nano Lett.* **18**, 7194–7199 (2018).
12. Akram, M. & Erten, O. Skyrmions in twisted van der Waals magnets. *Phys. Rev. B* **103**, L140406 (2021).
13. Xiao, F., Chen, K. & Tong, Q. Magnetization textures in twisted bilayer CrX_3 (X = Br, I). *Phys. Rev. Res.* **3**, 013027 (2021).
14. Wang, C., Gao, Y., Lv, H., Xu, X. & Xiao, D. Stacking domain wall magnons in twisted van der Waals magnets. *Phys. Rev. Lett.* **125**, 247201 (2020).
15. Li, T. et al. Pressure-controlled interlayer magnetism in atomically thin CrI_3. *Nat. Mater.* **18**, 1303–1308 (2019).
16. Song, T. et al. Switching 2D magnetic states via pressure tuning of layer stacking. *Nat. Mater.* **18**, 1298–1302 (2019).
17. Chen, W. et al. Direct observation of van der Waals stacking-dependent interlayer magnetism. *Science* **366**, 983 (2019).
18. Klein, D. R. et al. Enhancement of interlayer exchange in an ultrathin two-dimensional magnet. *Nat. Phys.* **15**, 1255–1260 (2019).
19. Sivadas, N., Okamoto, S., Xu, X., Fennie, C. J. & Xiao, D. Stacking-dependent magnetism in bilayer CrI_3. *Nano Lett.* **18**, 7658–7664 (2018).
20. Li, S. et al. Magnetic-field-induced quantum phase transitions in a van der Waals magnet. *Phys. Rev.* **10**, 011075 (2020).
21. Yoo, H. et al. Atomic and electronic reconstruction at the van der Waals interface in twisted bilayer graphene. *Nat. Mater.* **18**, 448–453 (2019).
22. Kim, K. et al. van der Waals heterostructures with high accuracy rotational alignment. *Nano Lett.* **16**, 1989–1995 (2016).
23. Cao, Y. et al. Superlattice-induced insulating states and valley-protected orbits in twisted bilayer graphene. *Phys. Rev. Lett.* **117**, 116804 (2016).
24. Chung, T.-F., Xu, Y. & Chen, Y. P. Transport measurements in twisted bilayer graphene: electron–phonon coupling and Landau level crossing. *Phys. Rev. B* **98**, 035425 (2018).
25. Jiang, S., Li, L., Wang, Z., Mak, K. F. & Shan, J. Controlling magnetism in 2D CrI_3 by electrostatic doping. *Nat. Nanotechnol.* **13**, 549–553 (2018).
26. Huang, B. et al. Electrical control of 2D magnetism in bilayer CrI_3. *Nat. Nanotechnol.* **13**, 544–548 (2018).
27. Jiang, S., Shan, J. & Mak, K. F. Electric-field switching of two-dimensional van der Waals magnets. *Nat. Mater.* **17**, 406–410 (2018).
28. Chen, L. et al. Topological spin excitations in honeycomb ferromagnet CrI_3. *Phys. Rev.* **8**, 041028 (2018).
29. McGuire, M. A., Dixit, H., Cooper, V. R. & Sales, B. C. Coupling of crystal structure and magnetism in the layered, ferromagnetic insulator CrI_3. *Chem. Mater.* **27**, 612–620 (2015).
30. Akram, M. et al. Moiré skyrmions and chiral magnetic phases in twisted CrX_3 (X = I, Br, Cl) bilayers. *Nano Lett.* **21**, 6633–6639 (2021).
31. Zener, C. Classical theory of the temperature dependence of magnetic anisotropy energy. *Phys. Rev.* **96**, 1335–1337 (1954).
32. Niitsu, K., Tanigaki, T., Harada, K. & Shindo, D. Temperature dependence of 180° domain wall width in iron and nickel films analyzed using electron holography. *Appl. Phys. Lett.* **113**, 222407 (2018).

Methods

Device fabrication. We fabricated twisted bilayer CrI_3 devices by the tear-and-stack method[22–24] inside a glovebox with water and oxygen levels below 1 ppm. Monolayer CrI_3 was mechanically exfoliated from bulk CrI_3 crystals onto SiO_2/Si substrates and identified by its optical contrast under a microscope. One example is shown in Extended Data Fig. 1a. We picked up a part of the flake (the black dashed curve) from the substrate with a polydimethylsiloxane/polycarbonate stamp and then twisted the remaining part (the red dashed curve in Extended Data Fig. 1b) on the substrate by an angle θ that ranges from 0° to 60°. A fine angle control is achieved by using a high-precision rotation stage (Thorlabs PR01). Finally, we engaged the two monolayers to form a twisted bilayer (Extended Data Fig. 1c). The finished twisted bilayer was encapsulated by hBN and contacted with graphene electrodes. A subset of the samples also has extra few-layer graphene as top and bottom gate electrodes. The CrI_3 and hBN substrates are generally not angle-aligned. Because of the large lattice mismatch between CrI_3 (6.87 Å) and hBN (2.5 Å), the relative angle alignment between the two is probably unimportant. We also fabricated a small number of hBN-encapsulated samples and transferred these onto TEM windows made of 8-nm-thick amorphous SiO_2 membranes for the STEM studies. Thinner hBN substrates (<5 nm thick) are used to reduce the hBN diffraction intensity. All of the encapsulated samples are chemically stable. Measurements over multiple cycles can be performed without any sign of sample degradation. Extended Data Fig. 2 shows the polarization angle dependence of the Raman spectrum of two small-twist-angle samples measured in the cross-polarization configuration. Isotropic angle dependence is observed, consistent with the three-fold rotational symmetry of twisted bilayer CrI_3.

Effects of lattice and strain relaxation. Similar to twisted bilayer graphene[21] and transition metal dichalcogenides[33], lattice and strain relaxations are expected in twisted bilayer CrI_3, especially for small twist angle and large moiré period. The main effect is expected to expand the R-stacking region, which has lower ground state energy[19], and therefore increase the FM ratio in the sample. This effect is expected to diminish at larger twist angles—for example, near the critical angle where the moiré period is reduced to ~13 nm. Because we do not observe a substantial increase in the FM ratio in small-twist-angle samples (Fig. 3a), large-scale structural relaxation is unlikely in the range of twist angles examined in this study.

MCD measurements. Similar MCD measurements on 2D CrI_3 have been reported in earlier studies[15,25,27]. In short, an incident He–Ne laser beam (633 nm) was focused onto the sample plane to a diffraction-limited spot (~500 nm in diameter) under normal incidence using a microscope objective of high numerical aperture (~0.81). The polarization of the incident light was modulated between left and right circular polarization by a photoelastic modulator. The reflected light was collected by the same objective and directed to a biased photodiode. The a.c. and d.c. components of the reflected light were collected by a lock-in amplifier and a multimeter, respectively. The MCD signal is defined as the ratio of the a.c. to the d.c. signal. Because circularly polarized light is used to probe the magnetic state, the measurement is insensitive to potential optical birefringence in the sample due to unintentional uniaxial strain[33]. For the MCD measurements, we have avoided samples or regions of samples with visible defects such as trapped bubbles. For MCD imaging studies, we used a filtered tungsten halogen lamp output (centred at 633 nm with a bandwidth of ~10 nm) for broad-field illumination in the same set-up. Samples with few or no visible trapped bubbles were selected. The reflected light intensity from left- and right-handed illumination was collected to a charge-coupled device that produces an optical image of the sample. The MCD image at a given magnetic field is obtained by normalizing the difference between the two images by their sum.

Four-dimensional STEM imaging and image analysis. The twisted bilayer CrI_3 sample was imaged in an FEI F20 S/TEM at 200 kV using a 10 μm condenser aperture and a probe semiconvergence angle of ~1.5 mrad. The sample was imaged using the 4D STEM technique, in which an electron probe is stepped over a scan region and a full electron diffraction pattern is recorded at each pixel step. The final 4D dataset (2D diffraction pattern × 2D image) was then used to recover details about the local crystal structure over large fields of view. All 4D STEM imaging was done using the Electron Microscope Pixel Array Detector (EMPAD)[34]. The high dynamic range of the EMPAD (10^6:1) allows for the collection of both the direct and scattered electron beams. A real-space scan size of 256 × 256 pixels and an acquisition time of 3 ms pixel^{-1} were used.

The 4D STEM data were screened and processed using the Cornell Spectrum Imager[35]. Each 4D STEM dataset consists of a 2D real-space scan and a 2D diffraction pattern associated with each real-space pixel in that scan. Virtual dark-field images are created by masking a region of the diffraction pattern and summing over the contributions of each pixel in the mask to obtain the intensity of the real-space image. The average moiré periodicity was calculated from the fast Fourier transform (FFT) of one of the dark-field images. The FFT contains a pair of peaks arising from the real-space moiré. A line profile was taken through the FFT and Gaussian functions were fitted to the peaks in MATLAB. The moiré periodicity and uncertainty were taken to be the mean and one standard deviation from the Gaussian fit parameters. Using this method, the moiré period in Fig. 1d–f was found to be 18.3 ± 2.7 nm.

AF–FM domain wall width. We consider a model that involves an abrupt physical boundary between the monoclinic and rhombohedral stacking regions in the moiré superlattice of twisted bilayer CrI_3. The simple model is intended to provide an order-of-magnitude estimate of the experimental observations. Since the interlayer FM exchange interaction for rhombohedral stacking is predicted to be substantially stronger than the interlayer AF exchange interaction for monoclinic stacking[19], we assume the AF–FM domain walls can only form in the monoclinic stacking regions. The domain wall energy per moiré unit cell consists of three terms:

$$E_{\mathrm{DW}} \approx \pi^2 \left(\frac{a_{\mathrm{M}}}{\delta}\right) \frac{J_{\parallel}}{2} + \left(\frac{\delta a_{\mathrm{M}}}{2a^2}\right) (K + 2J_{\perp}) . \quad (1)$$

Here δ is the domain wall width and $\frac{\delta a_{\mathrm{M}}}{a^2} \approx N$ is the number of spins in the domain wall (per moiré unit cell). The first two terms, involving intralayer FM exchange $J_{\parallel}$ and magnetic anisotropy K, constitute the standard expression for the energy cost of forming domain walls in FM materials. They compete against each other: a larger $J_{\parallel}$ favours a wider domain wall; conversely, a larger K favours a narrower domain wall. The last term is the energy cost from interlayer exchange interactions in the monoclinic stacking regions. It can be evaluated from $\sum_{i=1}^{N} J_{\perp}(1 + \cos\phi_i) \approx \frac{NJ_{\perp}}{\pi} \int_0^{\pi} \mathrm{d}\phi\,(1 + \cos\phi)$, where ϕ is the angle between the top and bottom layer spins. Minimizing E_{DW} with respect to δ yields an expression for the domain wall width:

$$\delta \approx \pi \sqrt{\frac{J_{\parallel} a^2}{K + 2J_{\perp}}} . \quad (2)$$

This is analogous to the result for domain walls in FM materials, $\delta \approx \pi\sqrt{\frac{J_{\parallel} a^2}{K}}$, with the modification of $K \rightarrow K + 2J_{\perp}$. We estimate the domain wall width in CrI_3 to be about 4 nm at low temperatures, which is substantially smaller than $a_{\mathrm{M}} \approx 20$ nm. At higher temperatures (still below T_c), where the magnetic anisotropy energy K becomes negligible compared to $J_{\perp}$, the domain wall width becomes $\delta \approx \pi\sqrt{\frac{J_{\parallel} a^2}{2J_{\perp}}}$. Therefore, δ here is expected to have a much weaker temperature dependence compared to that in the FM materials.

Critical twist angle and interlayer exchange coupling. In the above model, the non-collinear magnetic ground state originates from the competing magnetic interactions between the formation of the AF–FM domain walls and the interlayer AF exchange in the monoclinic stacking regions. A non-collinear state is favoured only if the latter dominates. The energy gain per moiré unit cell from having AF domains in the monoclinic stacking regions is:

$$E_{\mathrm{AF}} \approx 2 f_{\mathrm{AF}} \left(\frac{a_{\mathrm{M}}}{a}\right)^2 J_{\perp} . \quad (3)$$

The energy cost per moiré unit cell from forming the domain walls, after substituting equation (2) into equation (1), is:

$$E_{\mathrm{DW}} \approx \pi \left(\frac{a_{\mathrm{M}}}{a}\right) \sqrt{J_{\parallel} (K + 2J_{\perp})} . \quad (4)$$

The non-collinear-to-collinear phase transition occurs when $E_{\mathrm{AF}} \approx E_{\mathrm{DW}}$. If the transition is tuned by the twist angle θ, we can obtain a critical angle by using $\frac{a}{a_{\mathrm{M}}} = 2\sin\frac{\theta}{2} \approx \theta$:

$$\theta_c \approx \frac{f_{\mathrm{AF}} J_{\perp}}{\sqrt{J_{\parallel} (K + 2J_{\perp})}} . \quad (5)$$

Alternatively, if the transition is tuned by varying $J_{\perp}$ through gating at a fixed twist angle θ, we can obtain a critical interlayer exchange by keeping the leading-order term:

$$J_{\perp c} \approx \theta \sqrt{J_{\parallel} K} / f_{\mathrm{AF}} . \quad (6)$$

Spin-flip transition field. The spin-flip transition field B_c for the AF domains in the non-collinear phase can be evaluated following similar consideration of the energetics. The application of an external magnetic field favours the collinear state. The magnetic energy per moiré unit cell of the monoclinic stacking regions for the collinear state is

$$E_{\mathrm{col}} \approx f_{\mathrm{AF}} \left(\frac{a_{\mathrm{M}}}{a}\right)^2 (J_{\perp} - 3\mu_{\mathrm{B}} B) . \quad (7)$$

The first term is the energy cost for having an interlayer FM configuration in the collinear state; and the second term is the Zeeman energy gain for the FM

state. On the other hand, the energy per moiré unit cell at the monoclinic stacking regions for the non-collinear state is

$$E_{\mathrm{ncol}} \approx E_{\mathrm{DW}} - f_{\mathrm{AF}} \left(\frac{a_{\mathrm{M}}}{a}\right)^2 J_{\perp}. \quad (8)$$

The first term is the energy cost for forming domain walls and the second term is the energy gain for having an interlayer AF configuration in the monoclinic stacking regions. The spin-flip transition field can be obtained by equating (7) and (8):

$$B_{\mathrm{c}} \approx \frac{2f_{\mathrm{AF}}J_{\perp} - \pi\left(\frac{a}{a_{\mathrm{M}}}\right)\sqrt{J_{\parallel}(K+2J_{\perp})}}{f_{\mathrm{AF}}\,(3\mu_{\mathrm{B}})}. \quad (9)$$

Data availability

The source data that support the findings of this study are available within the paper. Additional data are available from the authors upon reasonable request. Source data are provided with this paper.

References

33. Bai, Y. et al. Excitons in strain-induced one-dimensional moiré potentials at transition metal dichalcogenide heterojunctions. *Nat. Mater.* **19**, 1068–1073 (2020).
34. Tate, M. W. et al. High dynamic range pixel array detector for scanning transmission electron microscopy. *Microsc. Microanal.* **22**, 237–249 (2016).
35. Cueva, P., Hovden, R., Mundy, J. A., Xin, H. L. & Muller, D. A. Data processing for atomic resolution electron energy loss spectroscopy. *Microsc. Microanal.* **18**, 667–675 (2012).

Acknowledgements

This work was supported by the Air Force Office of Scientific Research MURI under award FA9550-18-1-0480 (device fabrication and TEM characterization) and FA9550-19-1-0390 (MCD measurements). It was partially supported by the National Science Foundation under DMR-1807810 (modelling) and the Cornell Center for Materials Research with funding from the NSF MRSEC program under DMR-1719875 (Raman and structural characterization). Funding for J.E.G. was provided by the Center for Emergent Materials: an NSF MRSEC under award number DMR-2011876. D.W. acknowledges financial support by the German Science Foundation (Deutsche Forschungsgemeinschaft, DFG) under fellowship number WE6480/1. K.F.M. acknowledges support from a David and Lucille Packard Fellowship. Growth of the hBN crystals was supported by the Elemental Strategy Initiative of MEXT, Japan and CREST (JPMJCR15F3), JST.

Author contributions

Y.X. fabricated the devices and performed the MCD measurements and analysis. A.R. and Y.-T.S. performed the TEM measurements and analysis under the guidance of D.A.M. S.J. provided assistance in the MCD measurements. K.L. performed the Raman measurements. D.W. and J.E.G. grew the bulk CrI_3 crystals. K.W. and T.T. grew the bulk hBN crystals. Y.X., K.F.M. and J.S. designed the scientific objectives and co-wrote the manuscript. All authors discussed the results and commented on the manuscript.

Competing interests

The authors declare no competing interests.

Additional information

Extended data are available for this paper at https://doi.org/10.1038/s41565-021-01014-y.

Supplementary information The online version contains supplementary material available at https://doi.org/10.1038/s41565-021-01014-y.

Correspondence and requests for materials should be addressed to Kin Fai Mak or Jie Shan.

Peer review information *Nature Nanotechnology* thanks Xin Lu and the other, anonymous, reviewer(s) for their contribution to the peer review of this work.

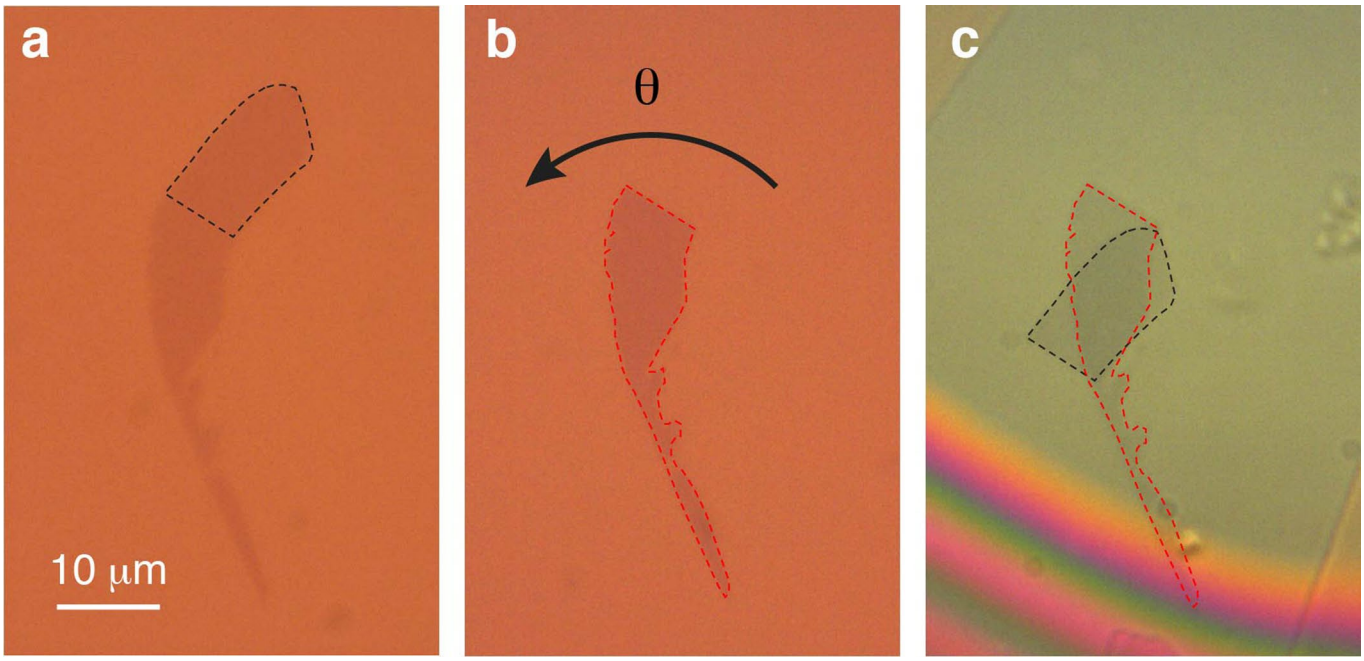

Extended Data Fig. 1 | Tear-and-stack method. a-**c**, Optical images taken during the preparation of a twisted bilayer CrI_3 sample. The monolayer in **a** is torn apart partially (outlined by the black dashed curves) and picked up by an hBN flake, leaving the remaining portion on the substrate. The remaining portion in **b** (outlined by the red dashed curves) is rotated by an angle θ. The two monolayers of CrI_3 are finally engaged to form a twisted bilayer (**c**). The scale bar is 10 micrometers.

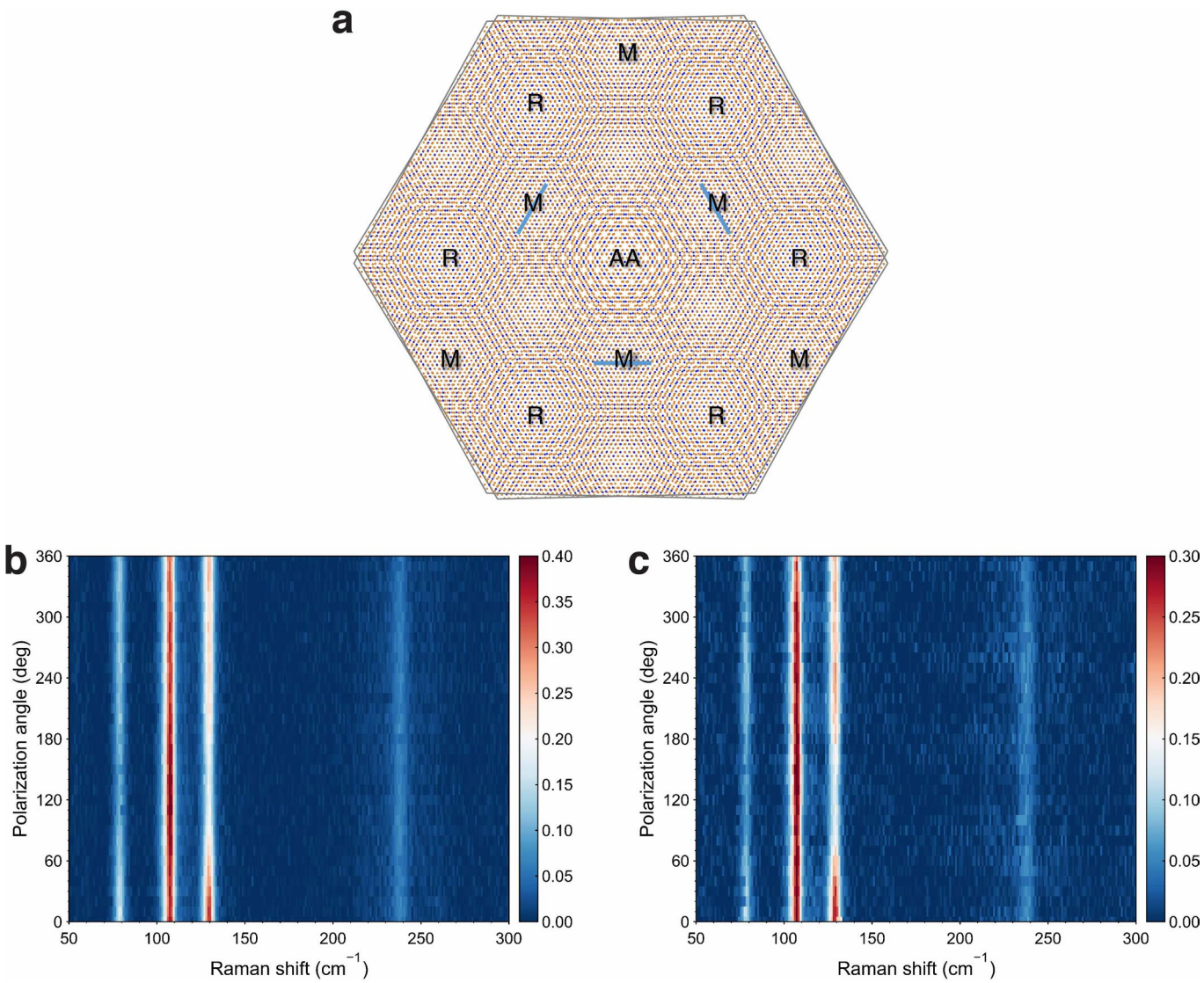

Extended Data Fig. 2 | Polarization-resolved Raman spectrum of twisted bilayer CrI_3. a, Schematics of a moiré superlattice structure formed by small-twist-angle bilayer CrI_3. R, M and AA denote rhombohedral, monoclinic and AA stacking order, respectively. The blue lines denote the direction of the major axis in the corresponding M region. The three axes are related to each other by a 120° rotation. **b,c**, Raman spectrum of a 1.2° (**b**) and a 2.0° (**c**) twisted bilayer as a function of polarization angle of the excitation. The linear polarization of the incident light is rotated by a half-wave-plate and cross-polarized Raman spectra are recorded. This is equivalent to recording cross-polarized Raman spectra for a rotating sample. Isotropic response is observed, as expected from the three-fold rotational symmetry of the major axis of the M regions.

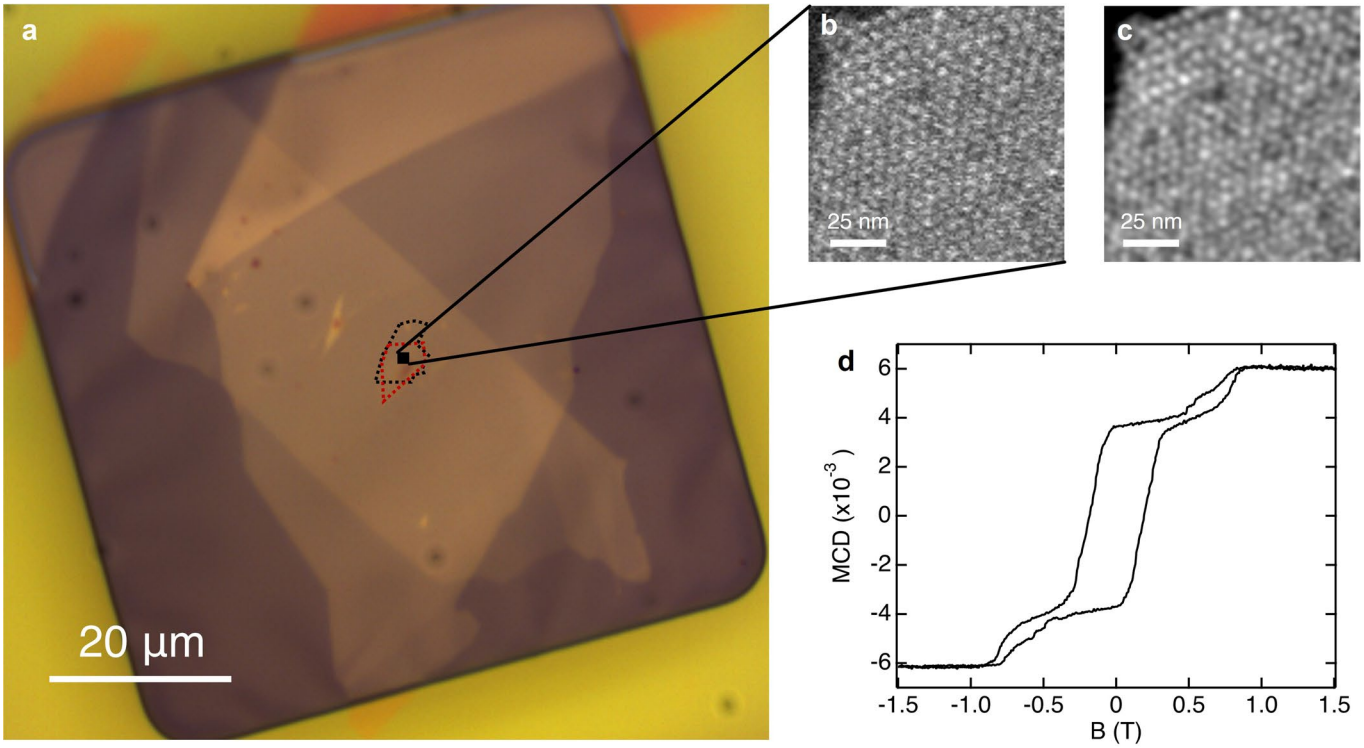

Extended Data Fig. 3 | Correlated STEM and MCD studies (sample 1). a, Optical image of the sample for the STEM measurements shown in Fig. 1. The scale bar is 20 micrometers. **b**,**c**, Sum of the STEM dark field images in Fig. 1d–f before (**b**) and after (**c**) applying a sigma=1.25 pixel Gaussian filter. Since the image is constructed from the third-order diffraction spots from twisted CrI_3, the true moiré period is three times the value shown in this figure. The scale bars are 25 nm. **d**, MCD measurement performed on the same sample area. No significant changes were observed in the MCD before and after the STEM measurements.

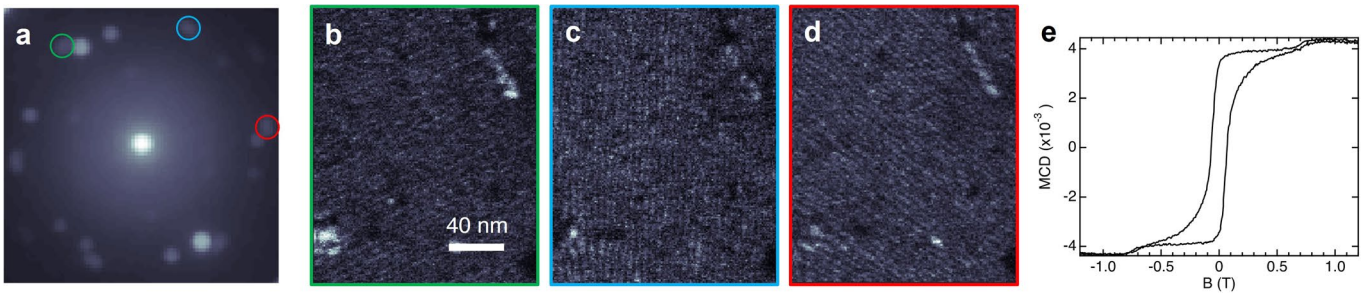

Extended Data Fig. 4 | Correlated STEM and MCD studies (sample 2). a-d, Electron diffraction and the corresponding real-space dark field moiré fringe patterns for sample 2, with the twist angle estimated to be 2.4 ± 0.5°. The target twist angle is 2°. **e**, MCD measurement performed on the same sample area.

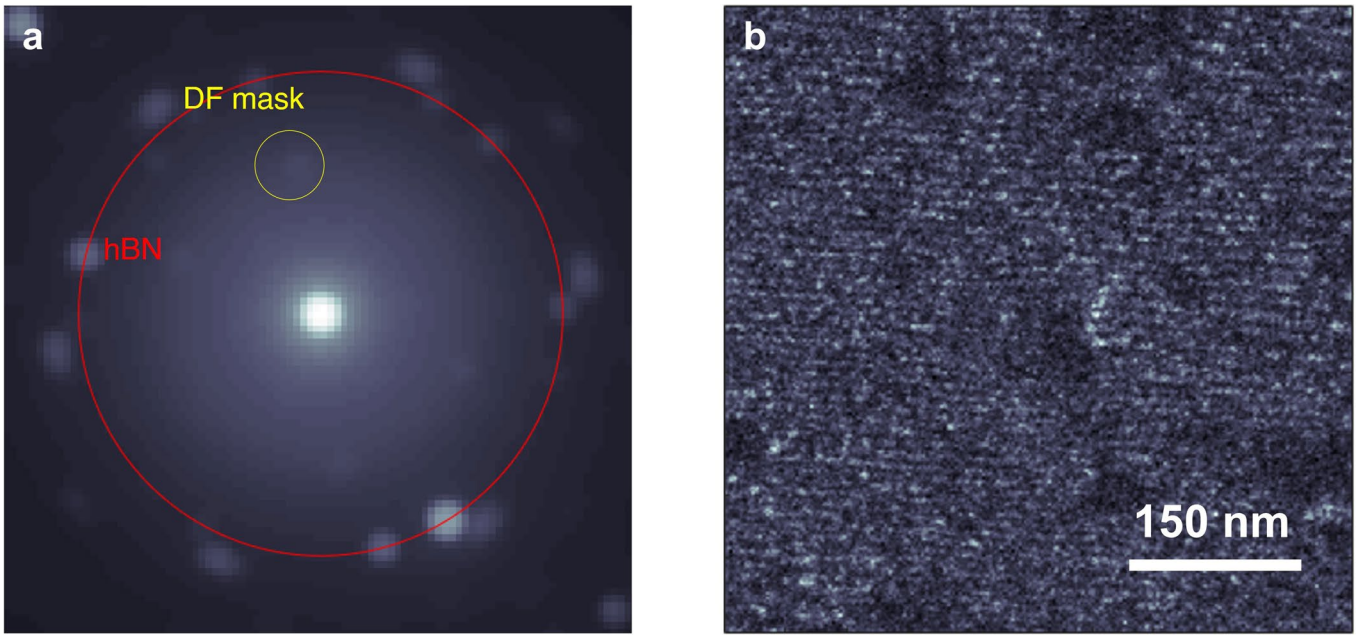

Extended Data Fig. 5 | Large field-of-view dark-field TEM image (sample 2). Electron-beam diffraction pattern (**a**) and real-space dark-field moiré fringe pattern (**b**). The image in **b** is constructed from the second-order diffraction peak of CrI_3 selected by the dark-field mask shown in yellow in **a**. The true moiré period is two times the value shown in **b**. The scale bar is 150 nm.

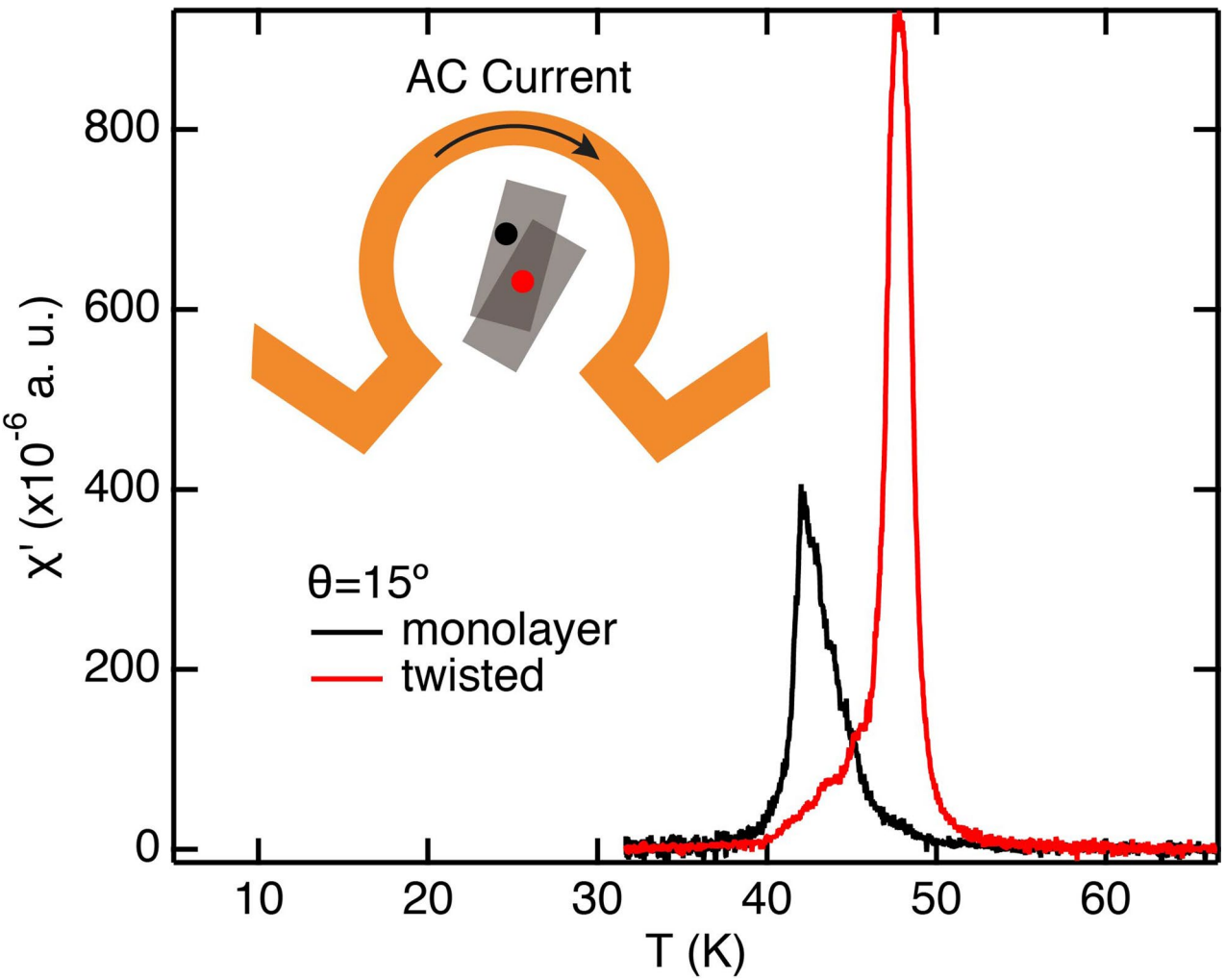

Extended Data Fig. 6 | Temperature dependent AC susceptibility (15°-twist sample). The inset shows the sample and the AC susceptibility measurement schematic. An AC current through the metallic ring structure is used to generate a small oscillating magnetic field of a few Oe. The AC susceptibility is measured using MCD as $\chi\prime = \frac{\partial MCD}{\partial H}$ (details of the method are described in ref. [25]). The twisted bilayer region (red) shows a single divergent peak of $\chi\prime(T)$, indicating FM coupling of the two layers and the absence of uncoupled regions. The Curie temperature is ~ 6 K higher in the twist bilayer than in the isolated monolayer region (black).

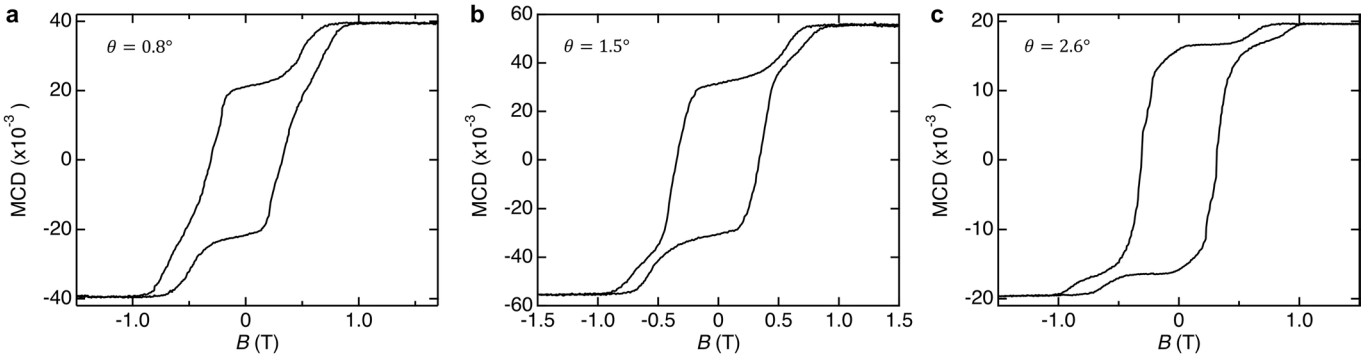

Extended Data Fig. 7 | Additional MCD data at 4 K for samples with twist angles 0.8° (**a**), 1.5° (**b**) and 2.6° (**c**).

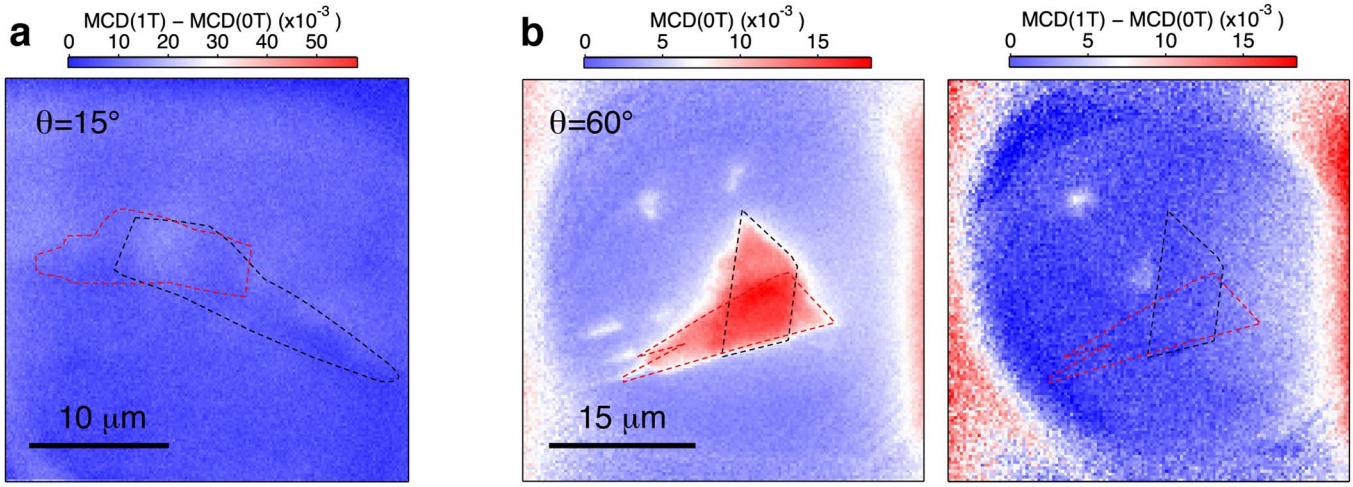

Extended Data Fig. 8 | Additional MCD imaging data. a, Map of *MCD*(1*T*) − *MCD*(0*T*) for 15°-twist bilayer CrI_3. No AF contribution is observed as expected. **b**, Map of *MCD*(0*T*) (left) and *MCD* (1*T*) − *MCD*(0*T*) (right) for a 60° sample. Only FM contribution is seen. The black and red dashed lines outline the constituent CrI_3 monolayers. The *MCD*(0T) image was taken after the sample is polarized at B = 1 T.

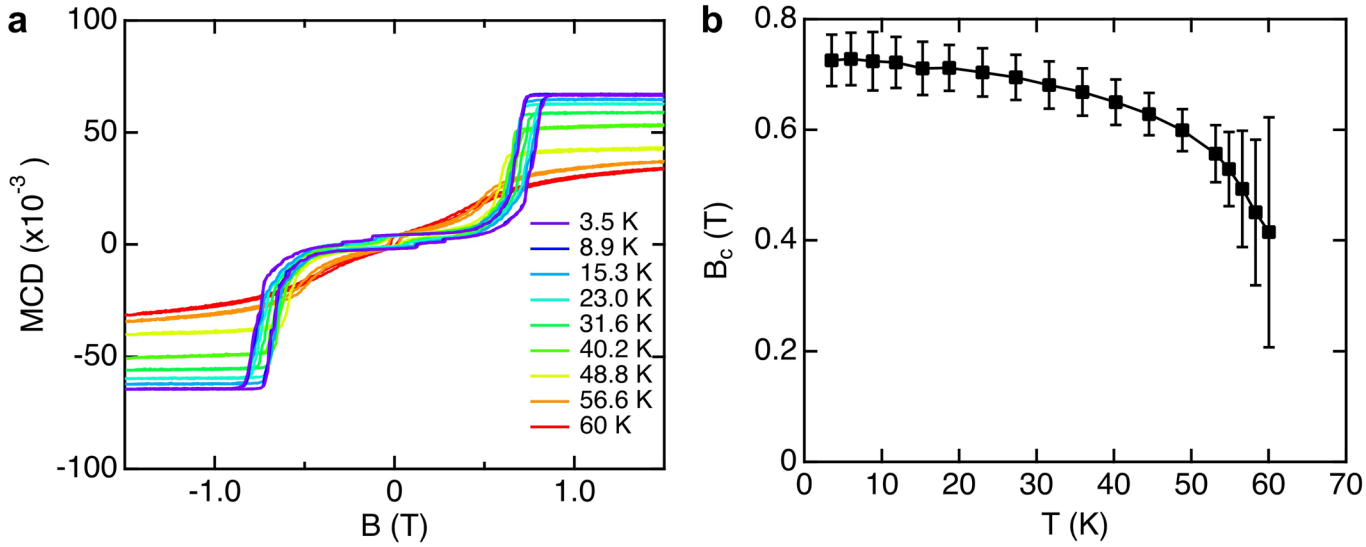

Extended Data Fig. 9 | Temperature dependence in natural bilayer CrI_3. MCD versus magnetic field in a natural bilayer CrI_3 at different temperatures (**a**) and the temperature dependence of the spin-flip transition field B_c (**b**). B_c is the average spin-flip transition field between forward and backward sweeps. The error bars are estimated from the width of the transition.

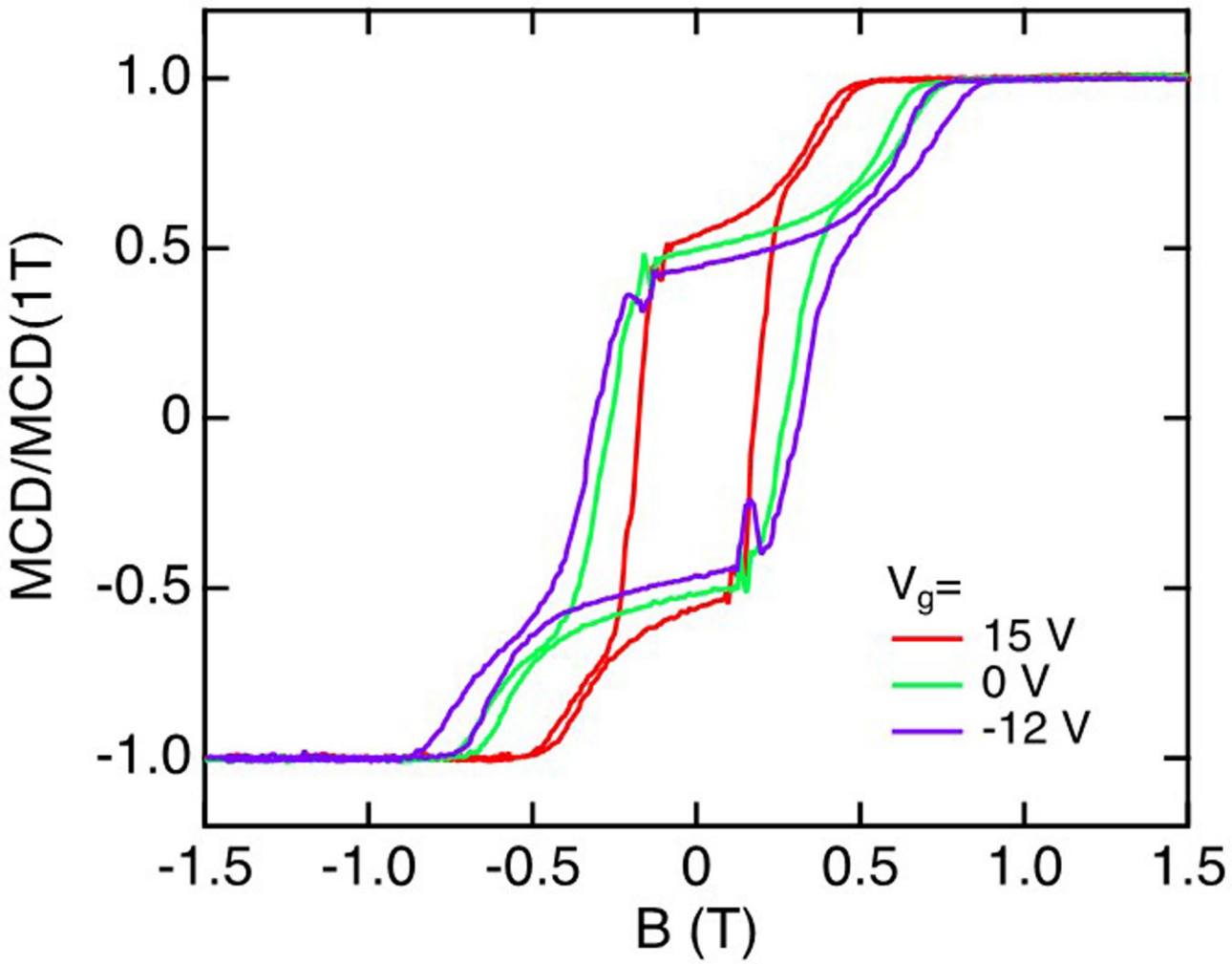

Extended Data Fig. 10 | Additional gate-dependent MCD response at 4 K for another sample with $\theta = 1.6°$.